Stretchable Supercapacitor at -30 ºC

Xuting Jin
Beijing Institute of Technology
Li Song
Beijing Institute of Technology
Hongsheng Yang
Beijing Institute of Technology
Chunlong Dai
Beijing Institute of Technology
Yukun xiao
Beijing Institute of Technology
Xinqun Zhang
Beijing Institute of Technology
Yuyang Han
Beijing Institute of Technology
Congcong Bai
Beijing Institute of Technology
Bing Lu
Beijing Institute of Technology
Qianwen Liu
Beijing Institute of Technology
Jiatao Zhang
Beijing Institute of Technology
Zhipan Zhang
Beijing Institute of Technology
Liangti Qu (lqu@tsinghua.edu.cn)
Tsinghua University https://orcid.org/0000-0002-0161-3816

Article

Keywords: supercapacitors, temperature tolerance, stretchability, anti-drying ability, processability

Posted Date: November 23rd, 2020

DOI: https://doi.org/10.21203/rs.3.rs-100376/v1

Abstract

At relatively low temperature (e.g, -30 ^{o}C), most flexible supercapacitors that work well at room temperature will lose their stretchability due to the poor cold intolerance of conventional electrolytes and the absence of intrinsically stretchable electrodes. Herein, an anti-freezing and highly stretchable supercapacitor (AF-SSC) was fabricated for the first time by one-step *in-situ* growth of polyaniline onto an organohydrogel polyelectrolyte from cross-linked polyacrylamide networks soaked by ethylene glycol/water/H_2SO_4. As no extra stretchable substrates (e.g. elastic fiber, polydimethylsiloxane, rubber, etc.) or predefining stretchable structures (e.g. helical, spring, wrinkle, honeycombed structures etc.) are needed in such a design, the prepared AF-SSC shows a high mechanical stretchability of 200% under -30 ^{o}C and can be repeatedly stretched for 100 cycles without significant capacitance loss. Besides, an impressive capacitance retention of 73.1% at -30 ^{o}C is achieved when the current density increases by 20 times, which is much higher than those of stretchable supercapacitors based on pseudocapacitive materials that operated at room temperature. Furthermore, the device shows an ultralong lifespan with 91.7% capacitance retention after 100000 cycles at -30 ^{o}C, outperforming all stretchable supercapacitors reported previously. With other merits of high compressibility, strong adhesion, good processability and excellent anti-drying ability, the current device is an ideal power source to drive multi-functional electronic components in real-life scenarios.

Introduction

Stretchable supercapacitors (SSCs) have been intensively investigated to meet the urgent demand in powering stretchable electronics such as electronic textiles[1], electronic skins[2], and wearable health monitors[3] due to their high power density, fast rate of charge-discharge and long cycling lifetime[4, 5]. To date, most SSCs work on electrodes with predefined stretchable structures, such as wave-like[6, 7], bridge-island[8], cellular[9], helical[10, 11], and spring-like[12, 13] geometries. Unfortunately, they usually suffer from the mechanical mismatches between predesigned electrodes and gel electrolytes or the volume/mass increase caused by the addition of extra stretchable substrates without capacitance contribution [14, 15]. Alternatively, geometrically editable supercapacitors (SCs) have been developed to overcome the poor stretchability of conventional SCs based on polyvinyl alcohol (PVA) electrolytes and common electrodes [15], yet these SCs are incapable of enduring large and complex deformations perpendicular to the direction of strain [16]. Meanwhile, they still adopt the conventional sandwich-like device structure of laminating separately prepared electrolyte and electrodes, thus vulnerably suffering from sliding and delamination under large deformations. To address these issues, it is critical to construct integrated SSCs based on intrinsically stretchable electrodes and electrolytes. On the other hand, there are few studies reporting SSCs tested under sub-zero temperatures when the freezing of water content in conventional hydrogel electrolytes would significantly restrict ionic transport[17, 18]. And even fewer reliable approaches have been proposed to solve the poor stretchability of SSCs under these circumstances.

Recently, organohydrogel electrolytes based on ethylene glycol (EG)/water (W) or dimethyl sulfoxide (DMSO)/water (W) have been utilized to fabricate anti-freezing SCs or micro-SCs[18-22] since both EG and DMSO can reduce the saturated vapor pressure of water to decrease its freezing point and suppress the formation of ice crystallites[22, 23]. However, SCs with organohydrogel electrolytes are usually not stretchable[18-23]. Herein, an integrated SC with intrinsic stretchability at low temperatures was fabricated for the first time by one-step *in-situ* growth of polyaniline electrodes onto an anti-freezing organohydrogel polyelectrolyte based on cross-linked polyacrylamide (PAM) networks impregnated by EG/W/H_2SO_4. Compared to conventional SSCs prepared with extra stretchable substrates or pre-defined stretchable structures, the current device is more convenient to fabricate and easier to control. Thanks to the intrinsic stretchability of PANI electrodes and anti-freezing nature of the organohydrogel PAM polyelectrolyte, the prepared SC can maintain 89.4% capacitance when stretched 200% at -30 ^{o}C. Benefiting from its integrated structure with highly efficient electron/ion transport, this device shows an excellent rate performance and achieves a high capacitance retention of 73.1% at -30 ^{o}C when the current density increases by 20 times, superior to those of the previously reported stretchable SCs with pseudocapacitive materials at room temperature. Furthermore, after 100000 cycles at 50 mV s^{-1} under -30 ^{o}C, this device displays an ultralong lifespan with 91.7% capacitance retention, exceeding that of all previously reported stretchable SCs. Remarkably, the device also has high compressibility, strong adhesion, good processability and excellent anti-drying ability.

Results

As illustrated in Fig. 1a and 1b, a chemically cross-linked polyacrylamide (C-PAM) hydrogel was synthesized by polymerizing acrylamide (AM) monomers in the presence of methylene-bis-acrylamide (BIS) as the cross-linking moiety, N, N, N', N'-tetramethylethylenediamine (TMED) as the catalyst and ammonium persulfate (APS) as the initiator. Then, a simple solvent displacement strategy was adopted to prepare an anti-freezing organohydrogel polyelectrolyte (AF-OHP) by immersing the C-PAM hydrogel in a mixed EG/W/H_2SO_4 solution. In supplementary Fig. 1, AF-OHP shows outstanding compression and excellent stretchability even when the temperature drops to -30 °C since EG can combine W molecules into stable molecular clusters and compete with the formation of hydrogen bonds between water molecules, resulting in the decrease of the saturated vapor pressure of W in EG/W binary solvents[23, 24]. Subsequently, an anti-freezing, intrinsically stretchable and truly integrated SC (AF-SSC) was fabricated by one-step *in-situ* growth of PANI electrodes onto both sides of the AF-OHP (Fig. 1a) with the transparent AF-OHP (6 cm in diameter) turing dark green (Fig. 1c). Unless otherwise specified, the fabricated SSC was based on the polyelectrolyte with an EG/W volume ratio of 1:1 due to the optimal anti-freezing property (see supplementary Fig. 2). Owing to the superior mechanical property of PANI electrodes and the AF-OHP, the AF-SSC could be arbitrarily deformed in forms of compressing, stretching, bending, and twisting (Fig. 1d). Meanwhile, it was also convenient to cut the AF-SSC into smaller SSCs of different shapes (Supplementary Fig. 3) or even shape it into numerical, cartoonish and alphabetic patterns (Figure 1e, 1f

and 1g). Overall, the high stretchability, excellent anti-freezing performance and outstanding processibility of the AF-SSC make it suitable for powering multifunctional electronic devices with different dimensions.

PANI has been widely used in SCs because of its relatively high pseudocapacitance and conductivity[25]. In current work, the *in-situ* growth of PANI and the presence of plentiful micropores in the AF-OHP contribute to the free moving of protons within the PANI/AF-OHP/PANI layers during charging and discharging (Fig. 2a and Fig. 2c), leading to higher ionic conductivity (5.33 mS cm^{-1}) than previously reported stretchable polyelectrolytes[7, 18, 26, 27] and conventional PVA-based gel electrolytes[28-31] (Supplementary Fig. 4). The cross-section view of the AF-SSC showed the penetration of PANI into the AF-OHP (Fig. 2b) and the growth of PANI nanofibers was confirmed by the roughened surface morphology of the oven-dried AF-SSC as compared to the pure AF-OHP (Fig. 2d and Supplementary Fig. 5). Meanwhile, the presence of the C-PAM and PANI components within the AF-SSC was further identified by their characteristic peaks in Fourier transform infrared (FTIR) and Raman spectra. In the FTIR spectrum of the C-PAM (Fig. 2e), the N–H stretching vibration peaks appear at 3346 cm^{-1} and 3189 cm^{-1} [32, 33], and the bands at 1645 cm^{-1} and 1602 cm^{-1} are attributed to the stretching of C=O and the bending of NH_2 from the amide group, respectively[36]. Due to the complexation of the C-PAM and PANI components in the AF-SSC, the N–H characteristic peaks at 3346 cm^{-1} and 3189 cm^{-1} in the C-PAM shift to 3432 and 3200 cm^{-1} in the AF-SSC. Besides, typical peaks of PANI at 1589 cm^{-1} (C=C stretching of the quinoid structure), 1496 cm^{-1} (C=C stretching of the benzenoid rings), 1165 cm^{-1} (electronic-like absorption of N=Q=N, where Q denotes the quinoid ring), and 817 cm^{-1} (aromatic ring deformation and C-H bond vibrations out of ring plane) are well resolved in the AF-SSC[34, 35]. Meanwhile, in the Raman spectrum of the AF-SSC (Fig. 2f), PANI bands at 1491 cm^{-1} (C=N stretching of the quinoid diimine units), 1585 cm^{-1} (C=C stretching of the quinoid rings), 1167 cm^{-1} (C-H bending of the quinoid rings), 1330 cm^{-1} (C-$N^{\bullet+}$ stretching) are also found[36]. In addition, compared to the amorphous feature of the C-PAM, the X-ray diffraction (XRD) pattern of the AF-SSC features characteristic peaks of crystallized PANI at 2θ of 18.3–30.9°, implying its high electrical conductivity (Fig. 2g)[37, 38]. All above characterizations indicate that PANI was successfully grown on both sides of the AF-OHP electrolyte, thus directly building a self-integrated SSC.

Interestingly, the AF-SSC maintained the good intrinsic tackiness of organohydrogel polyelectrolyte, making the device easily adhered to different substrates, including glass, polytetrafluoroethylene (PTFE), rubber gloves and polyethylene terephthalate (PET). In particular, the adhesive strength for rubber gloves could reach a maximum value of 10.4 KPa (Fig. 2i). On one hand, this enabled the direct attachment of current collectors (e.g. highly conductive carbon nanotube paper) without using additional conductive glues and an AF-SSC (~22 g, ~55 cm^2) could be easily lifted by a small piece of carbon nanotube paper (9.2 mg, 2390 times lighter in weight) on a small contact area of ~2.2 cm^2 (Fig. 2h and Supplementary Movie 1). On the other hand, the good tackiness and large deformability ensured a firm attaching of the AF-SSC on rubber gloves even under bending and stretching conditions for wearable electronics applications (Supplementary Fig. 6). The electrochemical performance of the AF-SSC was further assessed by cyclic voltammetry (CV) and galvanostatic charge-discharge (GCD) in a two-electrode

system. CV curves showed obvious redox peaks at scan rates ranging from 5 to 100 mV s^{-1}, originating from the characteristic pseudocapacitance behavior of PANI (Fig. 2j). GCD profiles were then measured at current densities ranging from 0.03 to 0.6 mA cm^{-2} to evaluate the specific capacitance of the device (Fig. 2k). Without any current collectors, the maximum specific areal capacitance of the AF-SSC still reached 14.4 mF cm^{-2} at 0.03 mA cm^{-2} and the corresponding IR drop was fairly small (Fig. 2l). Even when the current density increased by 20 times to 0.6 mA cm^{-2}, an impressive capacitance retention of 74.3% can be obtained (Fig. 2l). Alternatively, the specific capacitance of the device was also calculated by CV curves and its maximum areal capacitance can reach 12.8 mF cm^{-2} at 5 mV s^{-1} (Supplementary Fig. 7). Meanwhile, in the low frequency region of the electrochemical impedance spectrum (EIS), the close-to-vertical line demonstrated the good capacitive behavior of the AF-SSC without notable diffusion restrictions (Supplementary Fig. 8)[39]. The electrochemical stability of the AF-SSC was further investigated based on long-term CV tests at the scan rate of 100 mV s^{-1}. After 50000 cycles, 84.7 % of its initial capacitance was retained (Fig. 2m and Supplementary Fig. 9). Apart from PANI, poly (3, 4-ethylenedioxythiophene) (PEDOT) could also be *in-situ* grown on the AF-OHP by the same strategy to fabricate a control device. However, compared to PEDOT-based devices, the AF-SSC showed higher CV integral area, longer discharge time and better specific capacity, presumably owing to better pseudocapacitive behaviors of PANI (Supplementary Fig. 10).

As an indispensable component of SCs, the electrolyte plays an important role in determining the electrochemical performance and functionality of the device. Generally, hydrogel electrolytes tend to dry in 24 h due to inevitable evaporation of water under ambient conditions[40, 41], inducing deteriorations in ionic conductivity as well as mechanical properties (i.e. flexibility, stretchability, and compressibility). In contrast, this can be well avoided in the AF-SSC. When the AF-SSC and a control SC (CSC, prepared with the C-PAM hydrogel electrolyte) were intentionally stored in vacuum before testing, the AF-SSC still maintained good stretchability and compressive properties even after 20 h (Supplementary Fig. 11), showing a much smaller decrease in size and weight (Fig. 2n and Supplementary Fig. 12a). Specifically, after put in vacuum for 6h, 24h, and 48h, the solvent retention in the AF-SSC was 69.4%, 61.9 and 52.8%, respectively (Supplementary Fig. 12a). In contrast, only 22.7% of the solvent in the CSC remained after 6 h in vacuum (Supplementary Fig. 12a), which was even less than that (44.4%) of the AF-SSC after 72 h. Naturally, the AF-SSC maintained 70.6% and 64% of its initial capacitance after 6 h and 72 h under vacuum, while the capacitance of the CSC dropped to 47.2% only after 6 h (Fig. 2o and Supplementary Fig. 12b and 12c). This suggests that EG in AF-SSC forms a strong hydrogen bond network between polymer chains and water molecules, effectively preventing water molecules from volatilizing even under vacuum conditions.

The excellent stretchability of the AF-SSC originates from its rational structure. The penetration of PANI into the C-PAM organohydrogel warrants a high structural integrity and stable electrical conductivity under stretched states, since the external force could be evenly dissipated throughout the interconnected polymer network without causing interfacial separation between the electrode and the electrolyte (Fig. 3a). Consequently, the elongation of the AF-SSC could reach ~350% (Fig. 3b). Furthermore, CV and GCD

curves of the AF-SSC were barely changed under stretch ratios from 0% to 200% (Fig. 3c and Fig. 3d), while up to 93.9% and 84% of its original capacitance were retained when the device was stretched for 100% and 200% (Fig. 3e), respectively. In addition, the AF-SSC could be repetitively compressed to 80% of its original height and resistant to a maximum external pressure of 55.08 kPa for 100 cycles, demonstrating its stable elasticity. At the same time, the electrochemical performance of the AF-SSC was completely retained at various compressive strains from 0% to 60%, as indicated by CV and GCD curves (Fig. 3g and Supplementary Fig. 13a). Under 60% compression, its areal capacitance slightly increased by 9% (Fig. 3h), possibly due to pressure-improved interfacial contact between the electrolyte and electrodes[27, 42]. When the AF-SSC was repeatedly compressed to 60% and released for 1000 cycles, its CV and GCD curves barely changed (Fig. 3i and Supplementary Fig. 13b), with 99.9% and 96.3% of capacitance retained after 600 and 1000 compress/release cycles, respectively (Fig. 3j). Moreover, CV and GCD curves of the AF-SSC almost overlapped when the device was bent from 0° to 180° and its electrochemical performance only showed a negligible decay under large twisting (Supplementary Fig. 14).

Assembling individual SCs in series and parallel is an effective way to customize the output voltage and discharge capacity (Fig. 4a). Naturally, three series-connected and two parallel-connected AF-SSCs show tripled output voltage and doubled discharging time (Fig. 4b and 4c), respectively. A digital timer was sufficiently powered by three series-connected AF-SSCs even they were repeatedly stretched (Fig. 4d, Supplementary Movie 2), compressed (Fig. 4e, Supplementary Movie 2), bent or twisted (Fig. 4f and 4g). Owing to their good processability (Fig. 1e-1g), AF-SSCs with different alphabetic (Fig. 4h, Supplementary Movie 3) and numerical patterns (Fig. 4i, Supplementary Movie 3) can be facilely prepared to power a timer and a multifunctional displayer. Series-connected AF-SSCs can be directly adhered to rubber gloves and used to drive an electronic watch (Fig. 4j), validating that the AF-SSC features outstanding processability, good stickiness and excellent deformation adaptability for practical applications.

To date, most SSCs only maintain their high electrochemical performance at room temperature. Under -30 ^{o}C, water in the C-PAM hydrogel electrolyte (Fig. 5a) was frozen to ice and the CSC lost most of its electrochemical performance due to the greatly reduced ionic conductivity of the electrolyte and increased interfacial charge transfer resistance between the electrolyte and electrodes (Supplementary Fig. 15). In sharp contrast, the AF-SSC could work at this temperature (Fig. 5b and Fig. 5c). As shown in Fig. 5d and Supplementary Fig. 16, the electrochemical performance of the CSC significantly dropped under sub-zero temperatures, while the AF-SSC remained working at -30 ^{o}C. Such an excellent anti-freezing ability could be rationalized by the significantly higher ion conductivity of the AF-OHP (1.3 S m^{-1} at -30 ^{o}C) over that of the C-PAM hydrogel electrolyte (only 0.29 S m^{-1} even at -15 ^{o}C, Supplementary 17). Furthermore, CV and GCD experiments at 25 ^{o}C to -30 ^{o}C (Fig. 5g and Supplementary Fig. 18) showed that the AF-SSC maintained ~75% of its room temperature capacitance (Fig. 5h) with an excellent rate performance under -30 ^{o}C (Fig. 2k, Fig. 5i, and Supplementary Fig. 19). In details, the areal capacitance of AF-SSC was 14.4, 12.7, 11.5, and 10.4 mF cm^{-2} at 0.03 mA cm^{-2} under 25, 0, -15, and -30 ^{o}C, respectively (Fig. 5i). When the current density was increased by 20 folds to 0.6 mA cm^{-2} under 25, 0, -15, and -30 ^{o}C

(Fig. 5i), the corresponding areal capacitance slightly changed to 10.7, 9.3, 8.4, and 7.6 mF cm^{-2}, respectively, leading to unprecedented capacitance retention values (for instance, over 73% even at -30 ^{o}C) for stretchable supercapacitors in rate performance evaluations (Fig. 5j)[12, 15, 16, 43, 25, 43-48]. After 100000 change/discharge cycles at -30 ^{o}C, the AF-SSC maintained 91.7% of its initial capacitance (Fig. 5k, Supplementary Fig. 20), outperforming all available SSCs so far (Fig. 5l) [6, 15, 16, 25, 43, 44, 46-63].

To rationalize the anti-freezing mechanism of the AF-SSC, density functional theory (DFT) calculations with Dmol^3/GGA-PBE/DNP (3.5) basis set [1](3) were carried out to calculate the interaction energy of hydrogen bonds between C-PAM chains and EG as well as W molecules[23, 64]. As shown in Fig. 6a and 6b, hydrogen bonds form between small molecules such as W/W and W/EG. DFT results reveal that the hydrogen bonding interaction of EG–W mixture (-4.86 kcal mol^{-1}) in the AF-OHP is more stable than that of W–W (-3.74 kcal mol^{-1}) in the C-PAM hydrogel (Fig. 6c, d, and e, Supplementary Table1), which is crucial to maintain W molecules at low temperatures and thus enhance the cold tolerance of the AF-OHP [64]. Additionally, the EG–W mixture shows significantly stronger interactions (-23.15 kcal mol^{-1}) with PAM chains than pure W or EG (-9.68 or -4.98 kcal mol^{-1}, Fig 6f to 6h and Supplementary Table 2), where W molecules bridge to connect hydroxyl groups of the EG and carbonyl groups of PAM chains with an increased binding energy. As a result, water molecules are tightly locked in the AF-OHP network to suppress the formation of crystal lattices, enabling the AF-SSC to maintain good electrochemical performance at low temperatures.

The AF-SSC further exhibited a highly reversible stretchability at -30 ^{o}C (Fig. 7a). At -30 °C, its stress-strain curve was still similar to that measured at room temperature (Fig. 3b and Fig. 7b), proving the outstanding anti-freezing capacity and excellent stretchability of the AF-SSC. Electrochemically, the AF-SSC maintained typical pseudocapacitive CV curves (Fig. 7c) and GCD curves (Fig. 7d) even when stretched for 100% and 200% at -30 ^{o}C, with a high capacitance retention of up to 96.9% and 89.4%, respectively (Fig. 7e). After repeatedly stretched for 100 cycles at -30 ^{o}C, CV curves and GCD profiles of the AF-SSC showed no notable changes (Fig. 7f and 7g) and 94.8% of its initial capacitance was retained (Fig. 7h). As a proof-of-concept, three series-connected AF-SSCs could uninterruptedly power a timer at -30 ^{o}C even when one of them was repetitively stretched by 200% for three times (Fig. 7i, Fig. 7j and Supplementary Movie 4), highlighting their excellent anti-freezing and stretchable properties. As summarized in Fig. 7k and Supplementary Table 3, without the need of additional stretchable substrates or pre-existing stretchable structures, the AF-SSC achieved an unprecedented low-temperature intrinsic stretchability and an ultralong cycle lifespan[6, 7, 12, 15, 16, 25, 27, 43-63, 65-68]. In addition, the device simultaneously demonstrated high compression performance, strong stickiness, good processability and excellent anti-drying ability (Supplementary Table 3), qualifying it as a suitable candidate for wide applications in multifunctional wearable devices.

Discussion

In conclusion, we have developed an integrated supercapacitor with intrinsic stretchability at -30 ^{o}C by *in-situ* growth to form polyaniline onto the anti-freezing organohydrogel polyelectrolyte. Based on its truly integrated structure with facilitated electron/ion transport, the device shows an excellent rate performance with a high capacitance retention (>73.1%) under -30 ^{o}C when the current density increases by 20 folds. Additionally, at -30 ^{o}C, the device achieves a maximum stretch ratio of 200% and possesses an ultralong lifetime of 100000 cycles (91.7% of its initiall capacitance retained afterwards). To the best of our knowledge, the current device is the first SSC with such an intrinsic and stable stretchability at low temperatures and its other attractive features including high compressibility, strong adhesion, good processability and outstanding anti-drying ability further promote its potential applications in stretchable and wearable electronics towards real-life thermal environments.

Methods

Synthesis of the anti-freezing organohydrogel polyelectrolyte and the cross-linked polyacrylamide hydrogel polyelectrolyte: First, 6 g of AM (Acros Organics) was dispersed in 20 mL deionized water under the ultrasonic condition and then methylene-bis-acrylamide (0.003 g, Energy Chemical) was added into the solution. Sequentially, 15 μL of N, N, N', N'-tetramethyl-ethylenediamine (TMED) catalysts (Energy Chemical) and 0.02 mg of ammonium persulfate (APS) (Sigma-Aldrich) initiators were added to initiate polymerization under stirring. Then, the mixed solution were quickly poured in plastic vessels. After sealing and then reacting at 50 ^{o}C for 24 h, the cross-linked polyacrylamide hydrogel was obtained. Then, the anti-freezing organohydrogel polyelectrolyte (AF-OHP) were obtained by soaking the dried gels in 10 wt% of sulfuric acid ethylene glycol/water (v:v=1:1) solution for 72 h to achieve the equilibrated state. The cross-linked polyacrylamide hydrogel polyelectrolyte was prepared by soaking the cross-linked polyacrylamide hydrogel in 10 wt% of sulfuric acid aqueous solution for the same time. Similarly, control polyelectrolytes with different proportion of ethylene glycol/water (v/v=0, 1/3, 3/1) are prepared through the aforementioned method similar to AF-OHP to construct control SCs.

Fabrication of the supercapacitors

First, 5 mmol of aniline monomer (Macklin) was added into the 30 mL of above-mentioned sulfuric acid ethylene glycol/water solution with the same the same proportion under stirring in 0 ^{o}C for 10 min. Then, 3.33 mmol of APS was dissolved in 20 mL of the same sulfuric acid ethylene glycol/water solution under stirring and ultrasonic conditions at 0 °C. Next, the crosslinked AF-OHP with different sizes was immersed into sulfuric acid ethylene glycol/water solution containing 5 mmol of aniline monomer for 0.5h. Then, as-prepared APS solution was added to initiate polymerization under stirring for 12h at the room temperature. Finally, an antifreezed, essentially stretchable and truly integrated SC (AF-SSC) was fabricated by cutting their edges of the obtained sandwich-like block with the deposited PANI onto the two-sided faces to avoid the short circuit. Similarly, the different contrasted SCs (CSC, CSC-1/3 and CSC-3/1) based on the prepared polyelectrolytes with different proportion of ethylene glycol/water (v/v=0, 1/3 and 3/1) were also fabricated through the aforementioned method similar to AF-SSC, respectively. We

utilize carbon nanotube paper (Chengdu Organic Chemicals Co. Ltd., Chinese Academy of Sciences, China) as wire to directly fixed on both ends of the device for testing due to the strong stickiness of AF-SSC. Similarity, an integrated SC based on other conductive polymer such as poly (3, 4-ethylenedioxythiophene) (PEDOT) (Alfa) by using a similar construction strategy.

Characterizations: The morphologies of the samples were observed and investigated by SEM (JSM-7500F). Raman spectra and FT-IR spectra were carried out by a Horiba JY HR-800 Raman spectrometer and a Bruker VERTEX 700 spectrometer, respectively. X-ray diffraction (XRD) were tested by adopting Netherlands 1,710 diffractometer with a Cu-Kα irradiation source (λ=1.54 Å). A material testing system (SHIMADZU AGS-X) and DMA 850 was used to record the mechanical tensile tests. The performance of the device at low temperatures was tested with the aid of a commercial cryogenic refrigerator (Guangzhou Aoxue Refrigeration Equipment Co., Ltd., China). The ionic conductivity of the polyelectrolyte can be calculated by the relationship: σ= L/(RA), where L is the height between the current collectors, A is the contact area (m^2) between the polyelectrolyte and the current collectors, and R is the resistance measured by sandwiching the polyelectrolyte between two Au plates as current collectors using a CHI 760E electrochemical workstation. GCD profiles, CV curves, and electrochemical impedance spectroscopy (EIS) measurements of SCs were obtained by using a CHI 760E electrochemical workstation in two electrode configuration. The specific capacitance (C) can be calculated according to the single electrode data following the formulae: C =I△t/(AU), C= , where △t , I, U, , v, and A is the the discharging time, the discharge current, and the voltage variation (excluding the IR drop), the integrated area of the CV curve, scan rate and the area of SC, respectively. The adhesiveness of the SC was characterized by a tensile-adhesion test using different substrate materials on a universal mechanical testing machine (SHIMADZU AGS-X), according to previous literature[64, 69].

Density Functional Theory (DFT) Calculations

The simulation was performed using the density functional theory program $DMol^3$ in Material Studio (Accelrys, San Diego, CA)[23, 64]. The physical wave functions were is extended in terms of numerical basis sets, $Dmol^3$ /GGA-PBE/DNP(3.5) basis set, which is comparable to 6-31G** basis sets. The core electrons are processed by the DFT semi-core pseudo potential. Perdew-Burke-Ernzerhof (PBE) generalized gradient approximation (GGA) is used to calculate exchange correlation energy. A Fermi smearing of 0.005 Ha (1 Ha = 27.211 eV) and a global orbital cutoff of 5.2 Å were utilized. The convergence criteria for geometric optimization and energy calculation were set as follows: (a) Self-consistent field tolerance was 1.0×10^{-6} Ha/atom; (b) Energy tolerance was 1.0×10^{-5} Ha/atom; (c) The maximum force tolerance was 0.002 Ha/Å; (d) The maximum displacement tolerance was 0.005Å.

Interaction energy calculation

The interaction energy (E_{int}) is obtained according to the following equation, which represents the intensity of the interaction between the various components in the system:

$$E_{int}=E_{total}-E_{component} \quad (1)$$

where E_{total} and $E_{component}$ represent the total energy of the system, and the energy of each component in the system, respectively. A negative Eads value corresponds to stable adsorption between components. More negative E_{int} represents a stronger interaction in the system.

Declarations

Acknowledgements

We acknowledge the financial support from the National Key R&D Program of China (2017YFB1104300, 2016YFA0200200), NSFC (No. 21774015, 22035005, 52073159), NSFC-MAECI (51861135202) and NSFC-STINT (21911530143).

Author contributions

T. J. and L.S. planned and designed the project. H. Y., C. D., Y. X., X. Z., Y. H., C. B., B. L., X.W., G.W. and Y.X. conducted all of the experiments. J. Z., Z. Z. and L. Q. wrote and modified the paper. All the authors discussed the data and the manuscript.

Competing interests

The authors declare no competing interests.

References

1. Matsuhisa, N. et al. Printable elastic conductors with a high conductivity for electronic textile applications. *Nat. Commun*. **6**, 7461 (2015).
2. Larson, C. et al. Highly stretchable electroluminescent skin for optical signaling and tactile sensing. *Science* **351**, 1071-1074 (2016).
3. Lee, H. et al. A graphene-based electrochemical device with thermoresponsive microneedles for diabetes monitoring and therapy. *Nat. Nanotechnol*. **11**, 566-572 (2016).
4. Zhang, Z. et al. Superelastic Supercapacitors with High Performances during Stretching. *Adv. Mater*. **27**, 356-362 (2015).
5. Lv, T., Yao, Y., Li, N. & Chen, T. Highly stretchable supercapacitors based on aligned carbon nanotube/molybdenum disulfide composites. *Angew. Chem., Int. Ed.* **55**, 9191-9195 (2016).
6. Li, H. et al. Ultrastretchable and superior healable supercapacitors based on a double cross-linked hydrogel electrolyte. *Nat. Commun.* **10**, 536 (2019).
7. Huang, Y. et al. An intrinsically stretchable and compressible supercapacitor containing a polyacrylamide hydrogel electrolyte. *Angew. Chem., Int. Ed.* **56**, 9141-9145 (2017).

8. Kim, D., Shin, G., Kang, Y., Kim, W. & Ha, J. Fabrication of a stretchable solid-state micro-supercapacitor array. *ACS Nano* **7**, 7975-7982 (2013).
9. Li, X., Li, H., Fan, X., Shi, X. & Liang, J. 3D-printed stretchable micro-supercapacitor with remarkable areal performance. *Adv. Energy Mater.* **10**, 1903794 (2020).
10. Choi, C. et al. Elastomeric and dynamic MnO_2/CNT core-shell structure coiled yarn supercapacitor. *Adv. Energy Mater.* **6**, 1502119 (2016).
11. Yu, J. et al. A high performance stretchable asymmetric fiber-shaped supercapacitor with a core-sheath helical structure. *Adv. Energy Mater.* **7**, 1600976 (2017).
12. Wang, S. et al. Highly stretchable and self-healable supercapacitor with reduced graphene oxide based fiber springs. *ACS Nano* **11**, 2066-2074 (2017).
13. Lu, Z., Foroughi, J., Wang, C., Long, H. & Wallace, G. Superelastic hybrid CNT/graphene fibers for wearable energy storage. *Adv. Energy Mater.* **8**, 1702047 (2018).
14. Qi, D. et al. Suspended wavy graphene microribbons for highly stretchable microsupercapacitors. *Adv. Mater.* **27**, 5559-5566 (2015).
15. Lv, Z. et al. Editable supercapacitors with customizable stretchability based on mechanically strengthened ultralong MnO_2 nanowire composite. *Adv. Mater.* **30**, 1704531 (2018).
16. Li, L. et al. Cryopolymerization enables anisotropic polyaniline hybrid hydrogels with superelasticity and highly deformation-tolerant electrochemical energy storage. *Nat. Commun.* **11**, 62 (2020).
17. Gao, H. et al. Adaptive and freeze-tolerant heteronetwork organohydrogels with enhanced mechanical stability over a wide temperature range. *Nat. Commun.* **8**, 15911 (2017).
18. Rong, Q., Lei, W., Huang, J. & Liu, M. Low temperature tolerant organohydrogel electrolytes for flexible solid-state supercapacitors. *Adv. Energy Mater.* **8**, 1801967 (2018).
19. Jin, X. et al. A cross-linked polyacrylamide electrolyte with high ionic conductivity for compressible supercapacitors with wide temperature tolerance. *Nano Research*, **12**,1199-1206 (2019).
20. Jin, X. et al. Flexible and high-performance microsupercapacitors with wide temperature tolerance. *Nano Energy* **64**, 103938 (2019) .
21. Li, Z. et al. Flexible and anti-freezing quasi-solid-state zinc ion hybrid supercapacitors based on pencil shavings derived porous carbon. *Energy Storage Mater* **28**, 307-314 (2020) .
22. Lu, C. & Chen X. All-temperature flexible supercapacitors enabled by antifreezing and thermally stable hydrogel electrolyte. *Nano Lett.* **20**, 1907-1914 (2020).
23. Mo, F. et al. A flexible rechargeable aqueous zinc manganese-dioxide battery working at −20 °C. *Energy Environ. Sci.* **12**, 706-715 (2019).
24. Kumar, R., Baskar, P., Balamurugan, K., Das, S. & Subramanian, V. On the perturbation of the H-Bonding interaction in ethylene glycol clusters upon hydration. *J. Phys. Chem. A* **116**, 4239-4247 (2012).
25. Li, P. et al. Stretchable all-gel-state fiber-shaped supercapacitors enabled by macromolecularly interconnected 3D graphene/nanostructured conductive polymer hydrogels. *Adv. Mater.* **30**, 1800124

(2018).

26. Liu, F., Wang, J. & Pan, Q. An all-in-one self-healable capacitor with superior performance. *J. Mater. Chem. A* **6**, 2500-2506 (2018).
27. Huang, Y. et al. A self-healable and highly stretchable supercapacitor based on a dual crosslinked polyelectrolyte. *Nat. Commun.* **6**, 10310 (2015).
28. Lv, Q. et al. Ultrafast charge/discharge solid-state thin-film supercapacitors via regulating the microstructure of transition-metal-oxide. *J. Mater. Chem. A* **5**, 2759-2767 (2017).
29. Yu, H. et al. Improvement of the performance for quasi-solid-state supercapacitor by using PVA-KOH-KI polymer gel electrolyte. *Electrochim Acta* **56**, 6881- 6886 (2011).
30. Kuan, M., Majid, S. & Arof, A. Dielectric and conduction mechanism studies of PVA-orthophosphoric acid polymer electrolyte. *Ionics* **13**, 231-234 (2007).
31. Fei, H., Yang, C., Bao, H. & Wang, G. Flexible all-solid-state supercapacitors based on graphene/carbon black nanoparticle film electrodes and cross-linked poly(vinyl alcohol)-H_2SO_4 porous gel electrolytes. *J. Power Sources* **266**, 488-495 (2014).
32. Liu, R. et al. Tough and highly stretchable graphene oxide/polyacrylamide nanocomposite hydrogels. *J. Mater. Chem.* **22**, 14160-14167 (2012).
33. Ghosh, P., Chakrabarti, A. & Siddhanta, S. Studies on stable aqueous polyaniline prepared with the use of polyacrylamide as the water soluble support polymer. *Eur. Polym. J.* **35**, 803-813 (1999).
34. Chen, S. & Lee, H. Structure and properties of poly(acrylic acid)-doped polyaniline. *Macromolecules* **28**, 2858-2866 (1995).
35. Gomes, E. & Oliveira, M. Chemical polymerization of aniline in hydrochloric acid (HCl) and formic acid (HCOOH) media. Differences between the two synthesized polyanilines. *American J Polm Sci* **2**, 5-13 (2012).
36. Pereira da Silva J. E., de Faria D. L. A., Cordoba de Torresi S. I., & Temperini M. L. A. Influence of thermal treatment on doped polyaniline studied by resonance raman spectroscopy. *Macromolecules* **33**, 3077-3083 (2000).
37. Pouget, J. P., Jozefowica, M. E., Epstein, A. J., Tang, X. & MacDiarmid, A. G. X-ray structure of PANI. *Macromolecules*, **24**, 779-789 (1991).
38. Tang Q, et al. Polyaniline/polyacrylamide conducting composite hydrogel with a porous structure. *Carbohydrate Polymers* **74**, 215-219 (2008).
39. Pan, L. et al. Hierarchical nanostructured conducting polymer hydrogel with high electrochemical activity. *Proc. Natl. Acad. Sci. USA* **109**, 9287-9292 (2012).
40. Wu, J. et al. An intrinsically stretchable humidity sensor based on anti-drying, self-healing and transparent organohydrogels. *Mater. Horiz.* **6**, 595-603 (2019).
41. Chen, F. et al. Rational fabrication of anti-freezing, non-drying tough organohydrogels by one-pot solvent displacement. *Angew. Chem., Int. Ed.* **30**, 6678-6681 (2018).

42. Liu, X., Wu, D., Wang, H. & Wang, Q. Self-recovering tough gel electrolyte with adjustable supercapacitor performance. *Adv. Mater.* **26**, 4370-4375 (2014).
43. Chen, C., Qin, H., Cong, H. & Yu S. A highly stretchable and real-time healable supercapacitor. *Adv. Mater.* **31**, 1900573 (2019).
44. Zhang, Q. et al. Stretchable fiber-shaped asymmetric supercapacitors with ultrahigh energy density. *Nano Energy* **39**, 219-228 (2017).
45. Sun, J. et al. High-performance stretchable yarn supercapacitor based on PPy@ CNTs@urethane elastic fiber core spun yarn. *Nano Energy* **27**, 230-237 (2016).
46. Park, H. et al. Dynamically stretchable supercapacitor for powering an integrated biosensor in an all-in-one textile system. *ACS Nano* **13**, 10469-10480 (2019).
47. Chen, X. et al. Smart, stretchable supercapacitors. *Adv. Mater.* **26**, 4444-4449 (2014).
48. Choi, C. et al. Improvement of system capacitance via weavable superelastic biscrolled yarn supercapacitors. *Nat. Commun.* **7**, 13811 (2016).
49. Lamberti, A., Clerici, F., Fontana, M. & Scaltrito, L. A highly stretchable supercapacitor using laser-induced graphene electrodes onto elastomeric substrate. *Adv. Energy Mater.* **6**, 1600050 (2016).
50. Yu, J. et al. A high performance stretchable asymmetric fiber-shaped supercapacitor with a core-sheath helical structure. *Adv. Energy Mater.* **7**, 1600976 (2017)
51. Yang, Z., Deng, J., Chen, X., Ren, J. & Peng, H. A highly stretchable, fiber-shaped supercapacitor. *Angew. Chem. Int. Ed.* **52**, 13453-13457 (2013).
52. Dong, K. et al. A highly stretchable and washable all-yarn-based self-charging knitting power textile composed of fiber triboelectric nanogenerators and supercapacitors. *ACS Nano* **11**, 9490-9499 (2017).
53. Yu, C., Masarapu, C., Rong, J., Wei, B. & Jiang, H. Stretchable supercapacitors based on buckled single-walled carbon-nanotube macrofilms. *Adv. Mater.* **21**, 4793-4797 (2009).
54. Wang, Y. et al. A highly elastic and reversibly stretchable all-polymer supercapacitor. *Angew. Chem. Int. Ed.* **58**, 15707-15711 (2019).
55. Huang, Y. et al. Super-high rate stretchable polypyrrole-based supercapacitors with excellent cycling stability. *Nano Energy* **11**, 518-525 (2015).
56. Cao, C. et al. Highly stretchable supercapacitors via crumpled vertically aligned carbon nanotube forests. *Adv. Energy Mater.* **9**, 1900618 (2019).
57. Zhang, Z. et al. Nitrogen-doped core-sheath carbon nanotube array for highly stretchable supercapacitor. *Adv. Energy Mater.* **7**, 1601814 (2017).
58. Zhou, Y. et al. $Ti_3C_2T_x$ MXene-reduced graphene oxide composite electrodes for stretchable supercapacitors. *ACS Nano* **14**, 3576-3586 (2020).
59. Lv, T., Yao, Y., Li, N. & Chen T. Highly stretchable supercapacitors based on aligned carbon nanotube/molybdenum disulfide composites. *Angew. Chem. Int. Ed.* **55**, 9191-9195 (2016).

60. Li, F., Chen, J., Wang, X., Xue, M. & Chen, G. Stretchable supercapacitor with adjustable volumetric capacitance based on 3D interdigital electrodes. *Adv. Funct. Mater.* **25**, 4601-4606 (2015).
61. Xu, P. et al. Stretchable wire-shaped asymmetric supercapacitors based on pristine and MnO_2 coated carbon nanotube fibers. *ACS Nano* **9**, 6088-6096 (2015).
62. Choi, C. et al. Microscopically buckled and macroscopically coiled fibers for ultra-stretchable supercapacitors. *Adv. Energy Mater.* **7**, 1602021 (2016).
63. Choi, C., Lee, J. M., Kim, S. H. & Kim, S. J. Twistable and stretchable sandwich structured fiber for wearable sensors and supercapacitors. *Nano Lett.* **16**, 7677-7684 (2016).
64. Han, L. et al. Mussel-Inspired adhesive and conductive hydrogel with long-lasting moisture and extreme temperature tolerance. *Adv. Funct. Mater.* **28**, 1704195 (2018).
65. Hong, S. et al. Stretchable electrode based on laterally combed carbon nanotubes for wearable energy harvesting and storage devices. *Adv. Funct. Mater.* **27**, 1704353 (2017)
66. Yu, J. et al. Omnidirectionally stretchable high performance supercapacitor based on isotropic buckled carbon nanotube films. *ACS Nano* **10**, 5204-5211 (2016).
67. Pana, Z. et al. All-in-one stretchable coaxial-fiber strain sensor integrated with high-performing supercapacitor. *Energy Storage Mater*, **25**, 124-130 (2020).
68. Meng, Y. et al. All-graphene core-sheath microfi bers for all-solid-state, stretchable fibriform supercapacitors and wearable electronic textiles. *Adv. Mater.* **25**, 2326-2331 (2013)
69. Han, L. et al. Polydopamine nanoparticles modulating stimuli-responsive PNIPAM hydrogels with cell/tissue adhesiveness. *ACS Appl. Mater. Interfaces* **8**, 29088-29100 (2016).

Figures

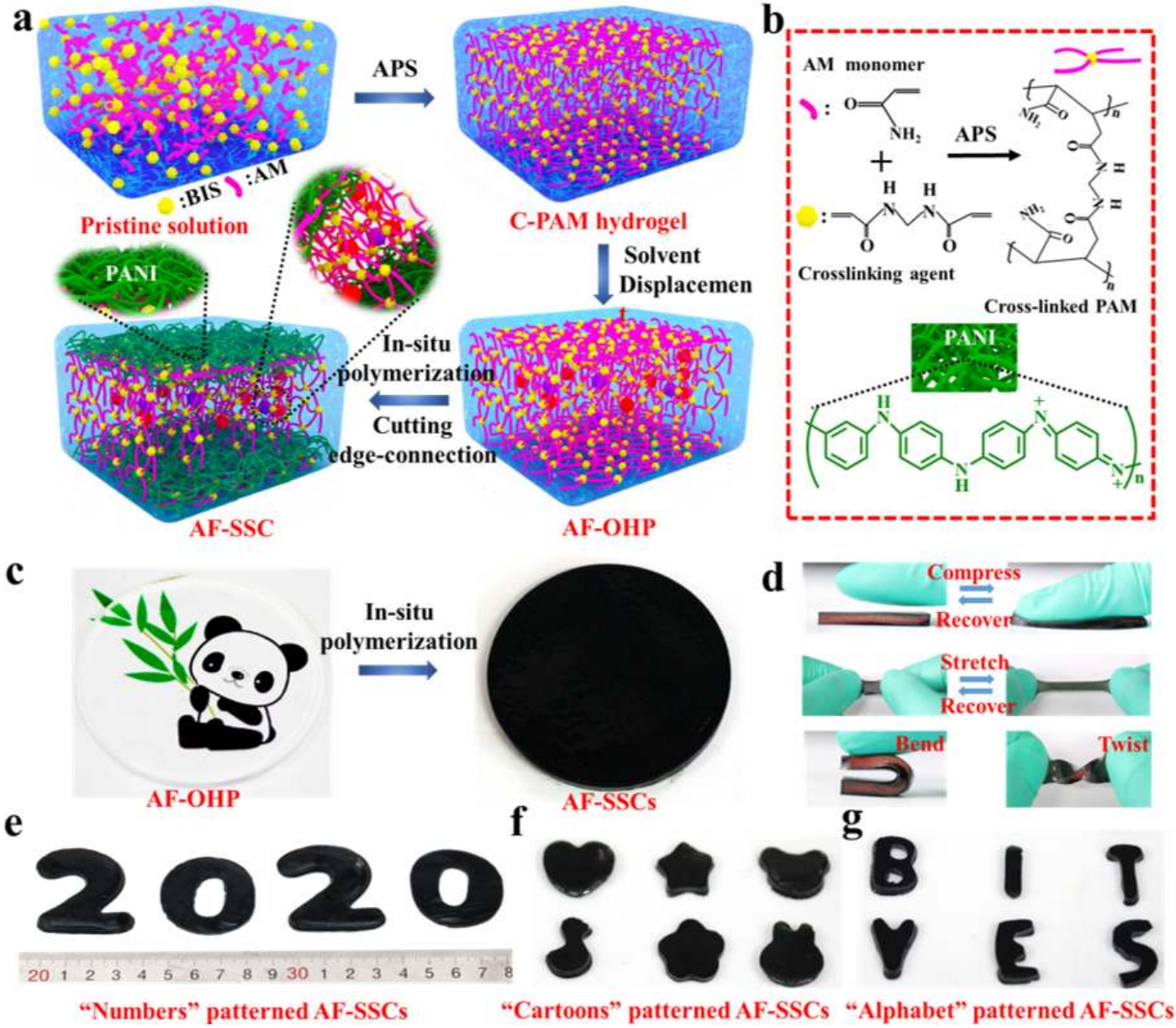

Figure 1

Fabrication and schematic of the AF-SSC. a) Schematic illustration of the preparation of AF-SSC. b) Chemical reaction process of cross-linked PAM and molecular structural formula of PANI. c) Optical image of dark green AF-OHP with PANI composite after in-situ polymerization. d) Optical images of the fabricated SC withstanding compressing, stretching, bending, and twisting deformations. Digital images of AF-SSC units with e) different numbers, f) cartoons and g) alphabet patterns.

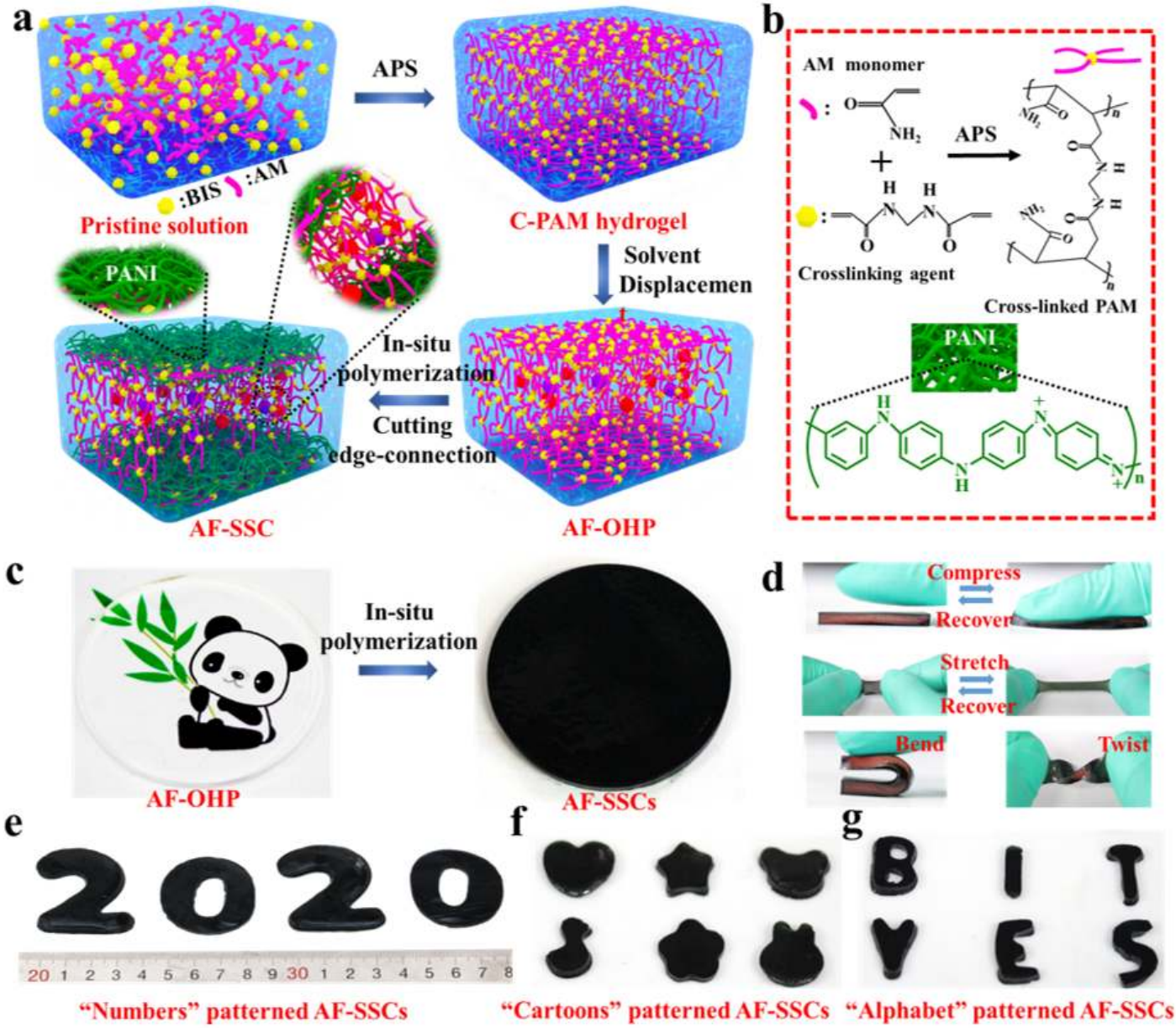

Figure 1

Fabrication and schematic of the AF-SSC. a) Schematic illustration of the preparation of AF-SSC. b) Chemical reaction process of cross-linked PAM and molecular structural formula of PANI. c) Optical image of dark green AF-OHP with PANI composite after in-situ polymerization. d) Optical images of the fabricated SC withstanding compressing, stretching, bending, and twisting deformations. Digital images of AF-SSC units with e) different numbers, f) cartoons and g) alphabet patterns.

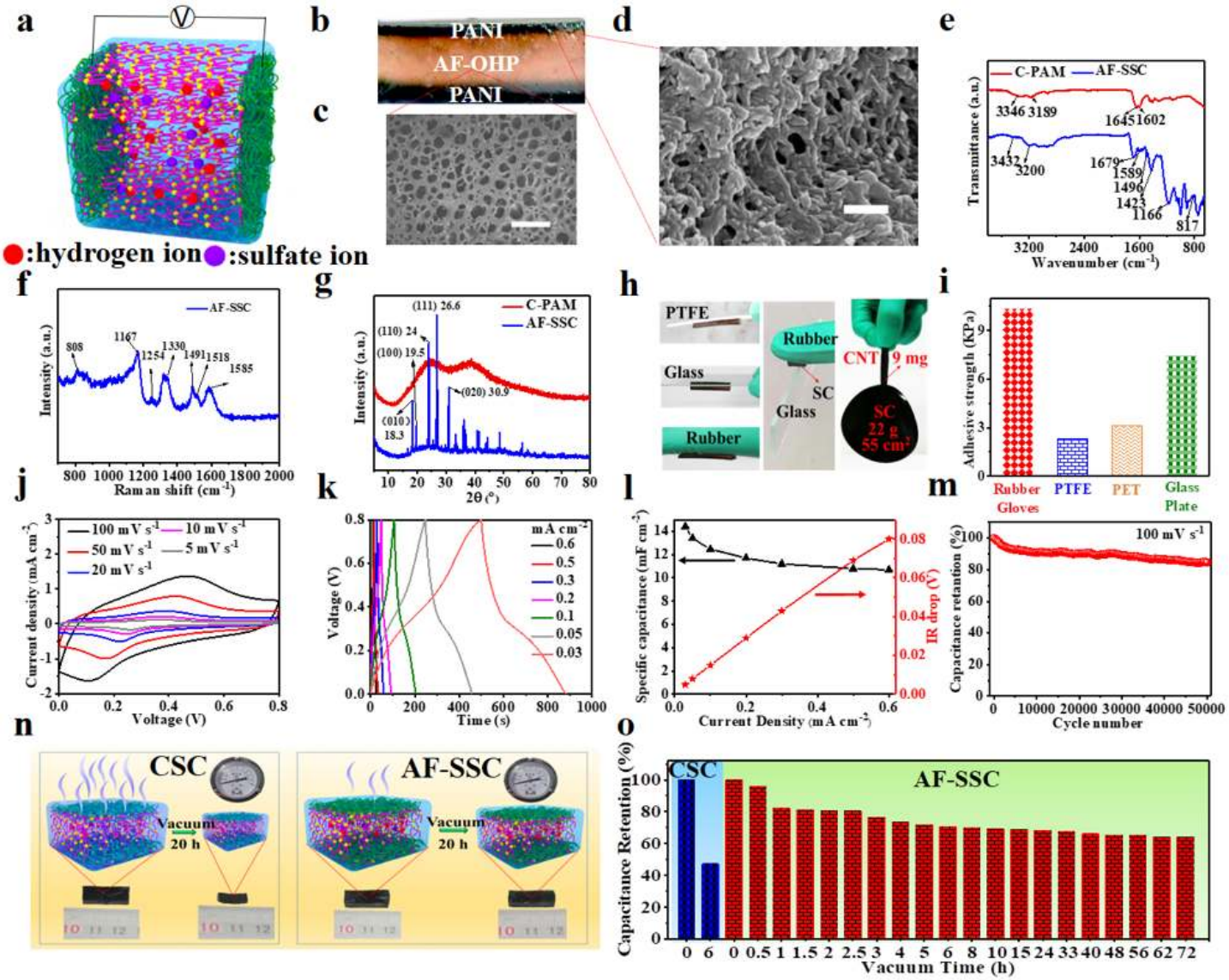

Figure 2

Structural characterization, adhesive property, anti-drying ability and electrochemical performance at room temperature of AF-SSC. a) Mechanism diagram and b) Optical picture of cross-section of AF-SSC. c) The SEM image of the freeze-dried C-PAM, Scale bar: 50 μm. d) The SEM image of PANI on the surface of oven-dried integrated SC, Scale bar: 400 nm. e) Fourier transform infrared spectra (FTIR), f) Raman spectra and g) X-ray diffraction (XRD) patterns of the C-PAM and AF-SSC. h) Optical picture and i) Adhesive strength of SCs adhered to different substrate surfaces; j) CV curves, k) GCD profiles, l) Specific capacitances and IR drop versus diverse current densities of the integrated devices. m) Capacitance retention at room temperature of AF-SSC during 50000 cycles. n) Diagram of change of AF-SSC and CSC under vacuum environment for 20 h; o) The capacitance retention at the scan rate of 50 mV s-1 of AF-SSC and CSC under vacuum environment for different time.

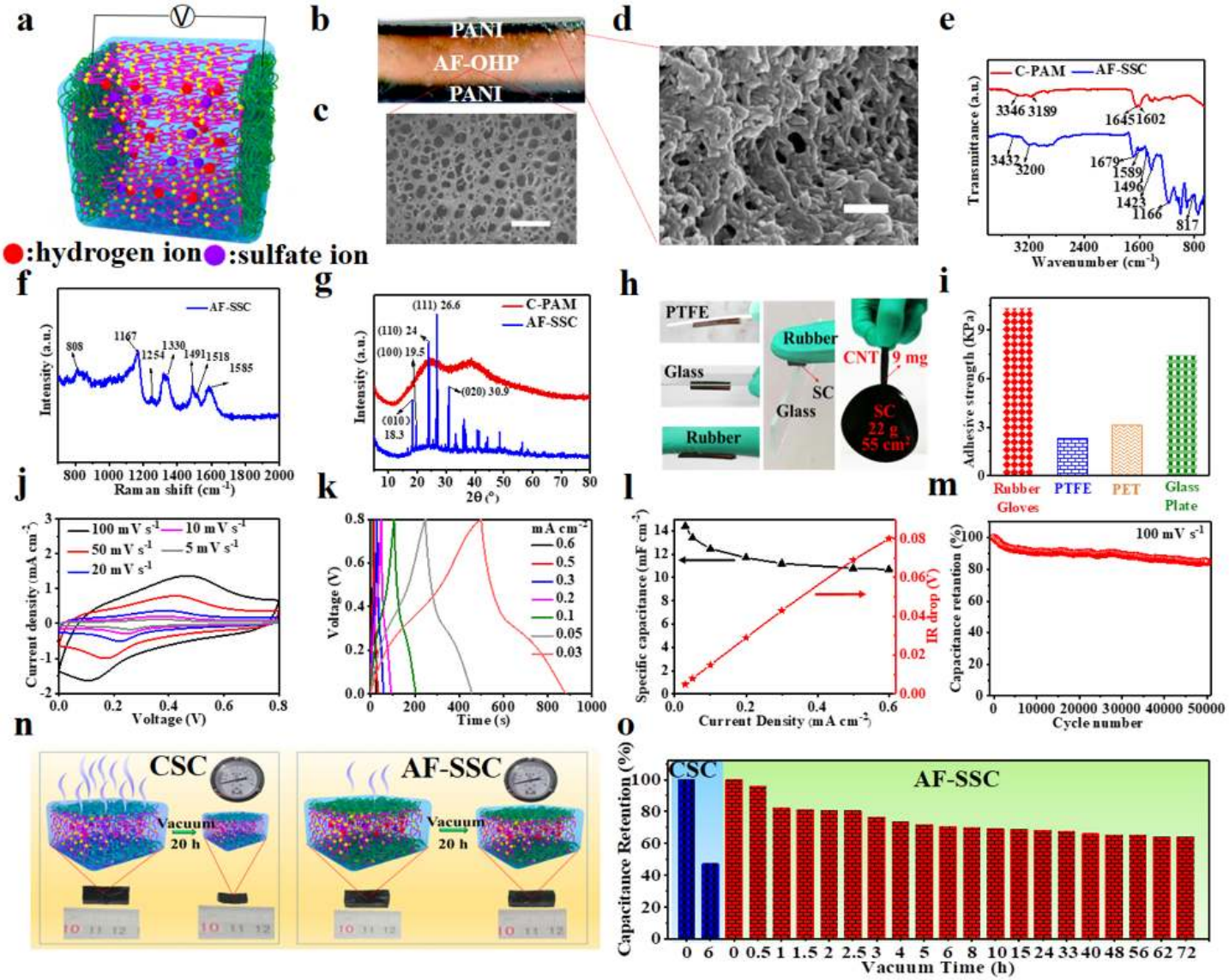

Figure 2

Structural characterization, adhesive property, anti-drying ability and electrochemical performance at room temperature of AF-SSC. a) Mechanism diagram and b) Optical picture of cross-section of AF-SSC. c) The SEM image of the freeze-dried C-PAM, Scale bar: 50 μm. d) The SEM image of PANI on the surface of oven-dried integrated SC, Scale bar: 400 nm. e) Fourier transform infrared spectra (FTIR), f) Raman spectra and g) X-ray diffraction (XRD) patterns of the C-PAM and AF-SSC. h) Optical picture and i) Adhesive strength of SCs adhered to different substrate surfaces; j) CV curves, k) GCD profiles, l) Specific capacitances and IR drop versus diverse current densities of the integrated devices. m) Capacitance retention at room temperature of AF-SSC during 50000 cycles. n) Diagram of change of AF-SSC and CSC under vacuum environment for 20 h; o) The capacitance retention at the scan rate of 50 mV s-1 of AF-SSC and CSC under vacuum environment for different time.

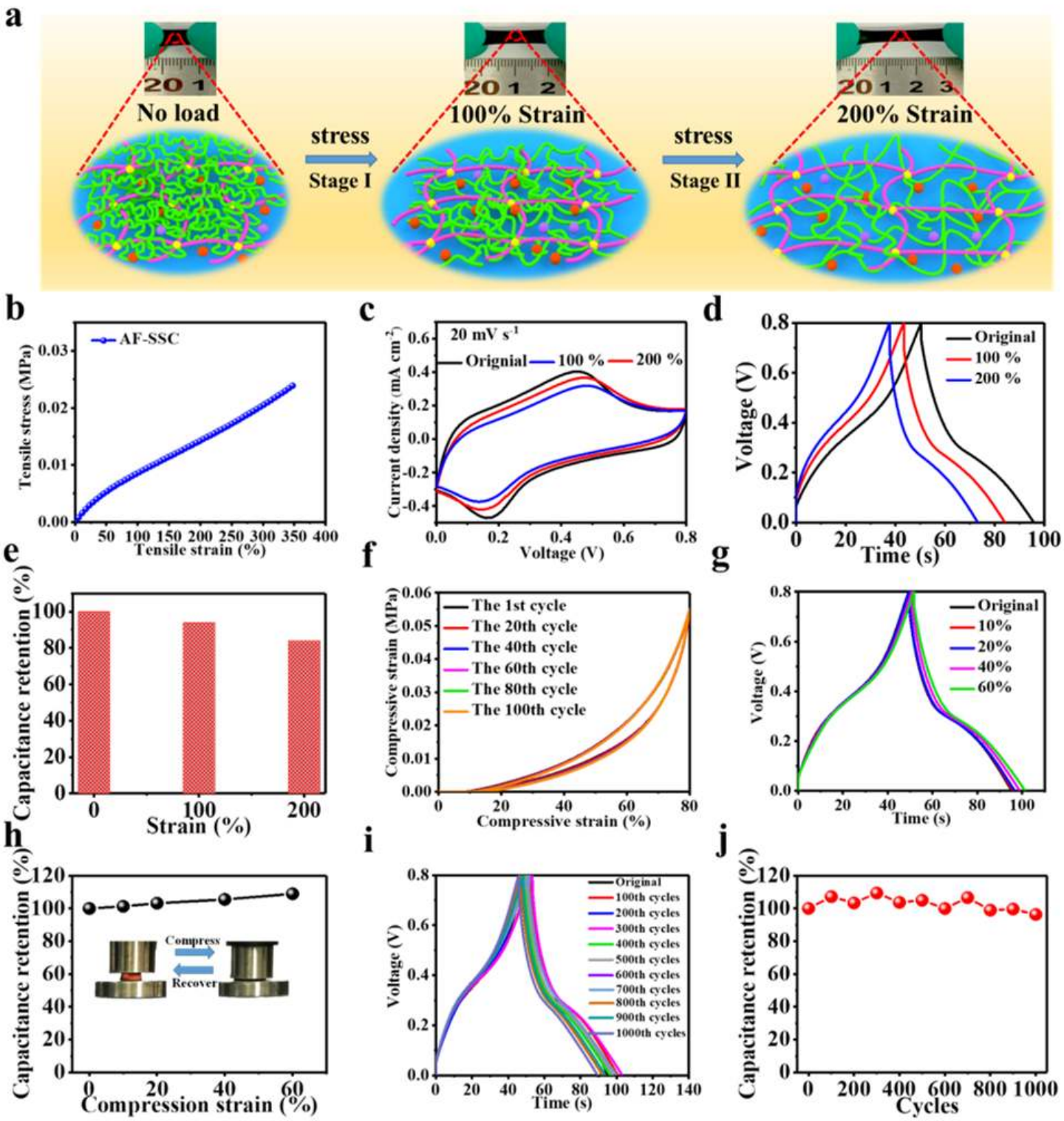

Figure 3

Performance of AF-SSC under large/complex deformation. a) Schematic illustration of the stretching process and b) Tensile stress-strain curve of AF-SSC. c) The CV curves at the scan rate of 20 mV s-1, d) GCD curves at the current density of 0.2 mA cm-2 and e) Capacitance retention of AF-SSC under different stretch ratio of AF-SSC. f) Cyclic compressive stress-strain curves at 80% compression strain of AF-SSC. g) GCD curves and h) Capacitance retention of AF-SSC at the current density of 0.2 mA cm-2 under

different compress ratio. i) GCD curves and j) Capacitance retention of AF-SSC at the current density of 0.2 mA cm-2 after different compress/release cycles from the initial to 60%.

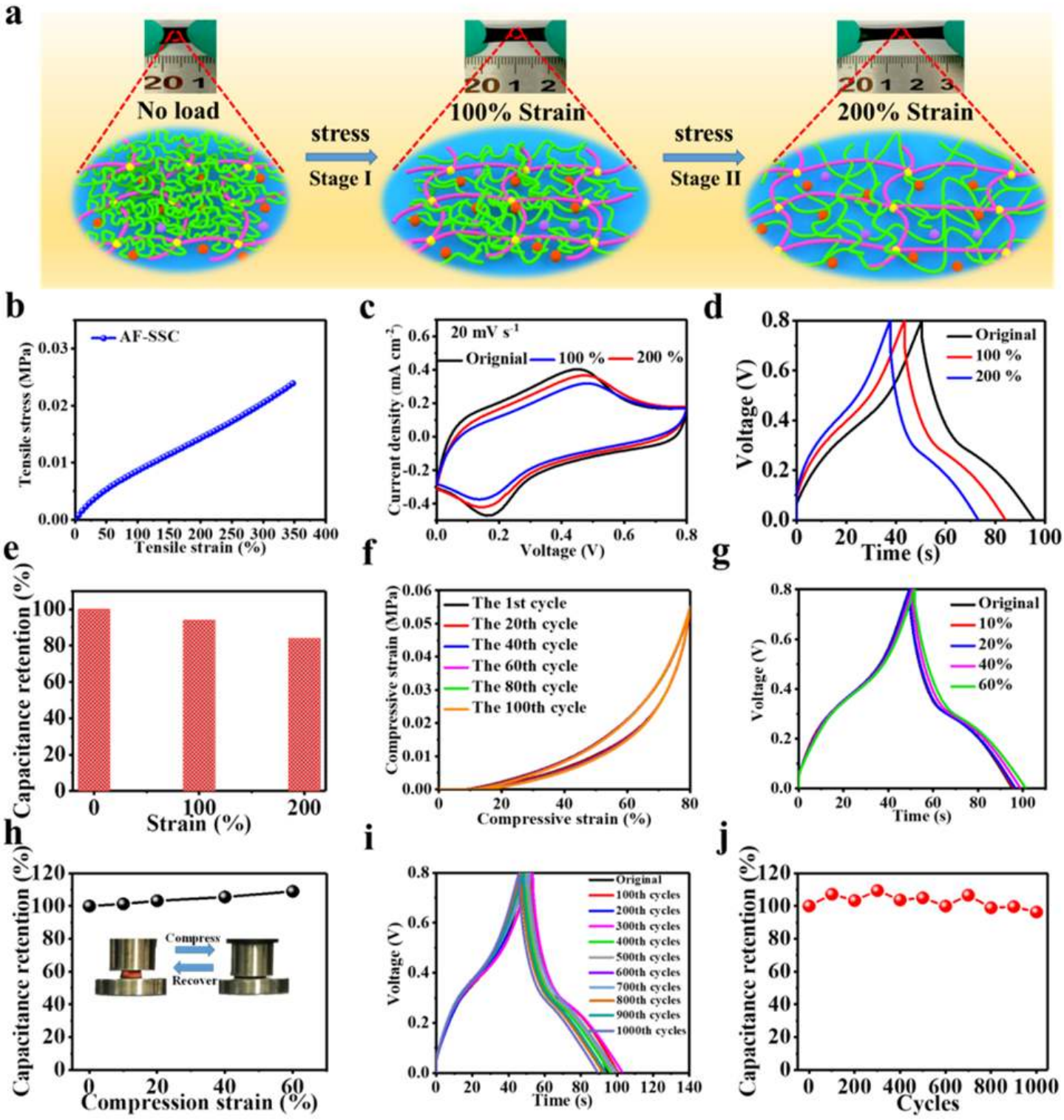

Figure 3

Performance of AF-SSC under large/complex deformation. a) Schematic illustration of the stretching process and b) Tensile stress-strain curve of AF-SSC. c) The CV curves at the scan rate of 20 mV s-1, d) GCD curves at the current density of 0.2 mA cm-2 and e) Capacitance retention of AF-SSC under different

stretch ratio of AF-SSC. f) Cyclic compressive stress-strain curves at 80% compression strain of AF-SSC. g) GCD curves and h) Capacitance retention of AF-SSC at the current density of 0.2 mA cm-2 under different compress ratio. i) GCD curves and j) Capacitance retention of AF-SSC at the current density of 0.2 mA cm-2 after different compress/release cycles from the initial to 60%.

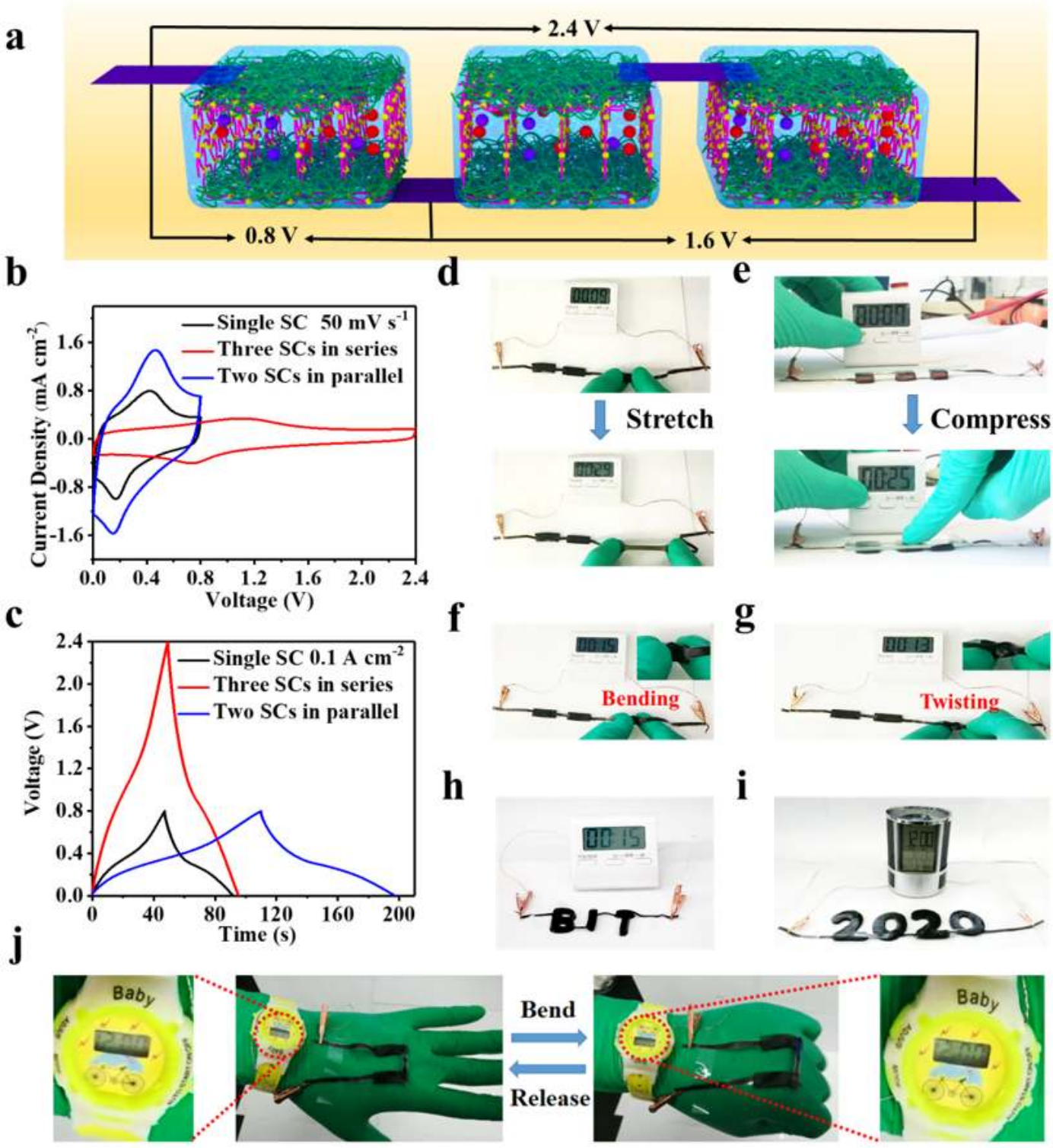

Figure 4

Performance of AF-SSCs with different patterns in series or parallel combinations under various deformation such as stretching, compressing, bending and twisting. a) Schematic illustration of three AF-SSCs connected in series. b) CV curves and c) GCD profiles of AF-SSCs connected in series or parallel. A commercialized timer powered by three AF-SSCs connected in series under d) stretching, e) compressing, f) bending and g) twisting. h) The timer driven by “BIT” patterned AF-SSCs assembled in series. i) A multifunctional pen holder displayer with music powered by “2020” patterned SCs assembled in series. j) An electronic watch powered by two in-series AF-SSCs firmly adhered to the rubber gloves under bending.

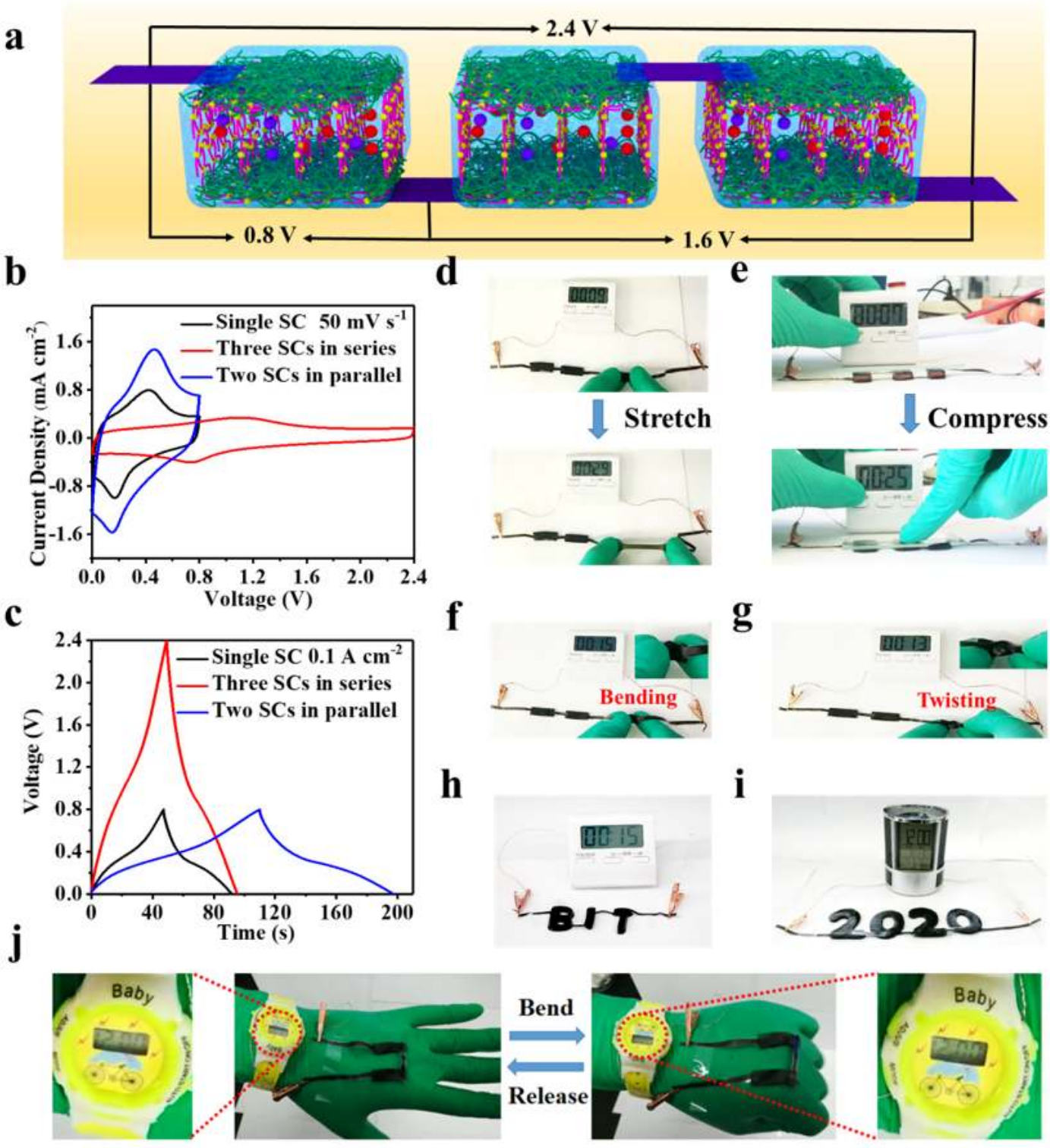

Figure 4

Performance of AF-SSCs with different patterns in series or parallel combinations under various deformation such as stretching, compressing, bending and twisting. a) Schematic illustration of three AF-SSCs connected in series. b) CV curves and c) GCD profiles of AF-SSCs connected in series or parallel. A commercialized timer powered by three AF-SSCs connected in series under d) stretching, e) compressing, f) bending and g) twisting. h) The timer driven by “BIT” patterned AF-SSCs assembled in series. i) A multifunctional pen holder displayer with music powered by “2020” patterned SCs assembled in series. j) An electronic watch powered by two in-series AF-SSCs firmly adhered to the rubber gloves under bending.

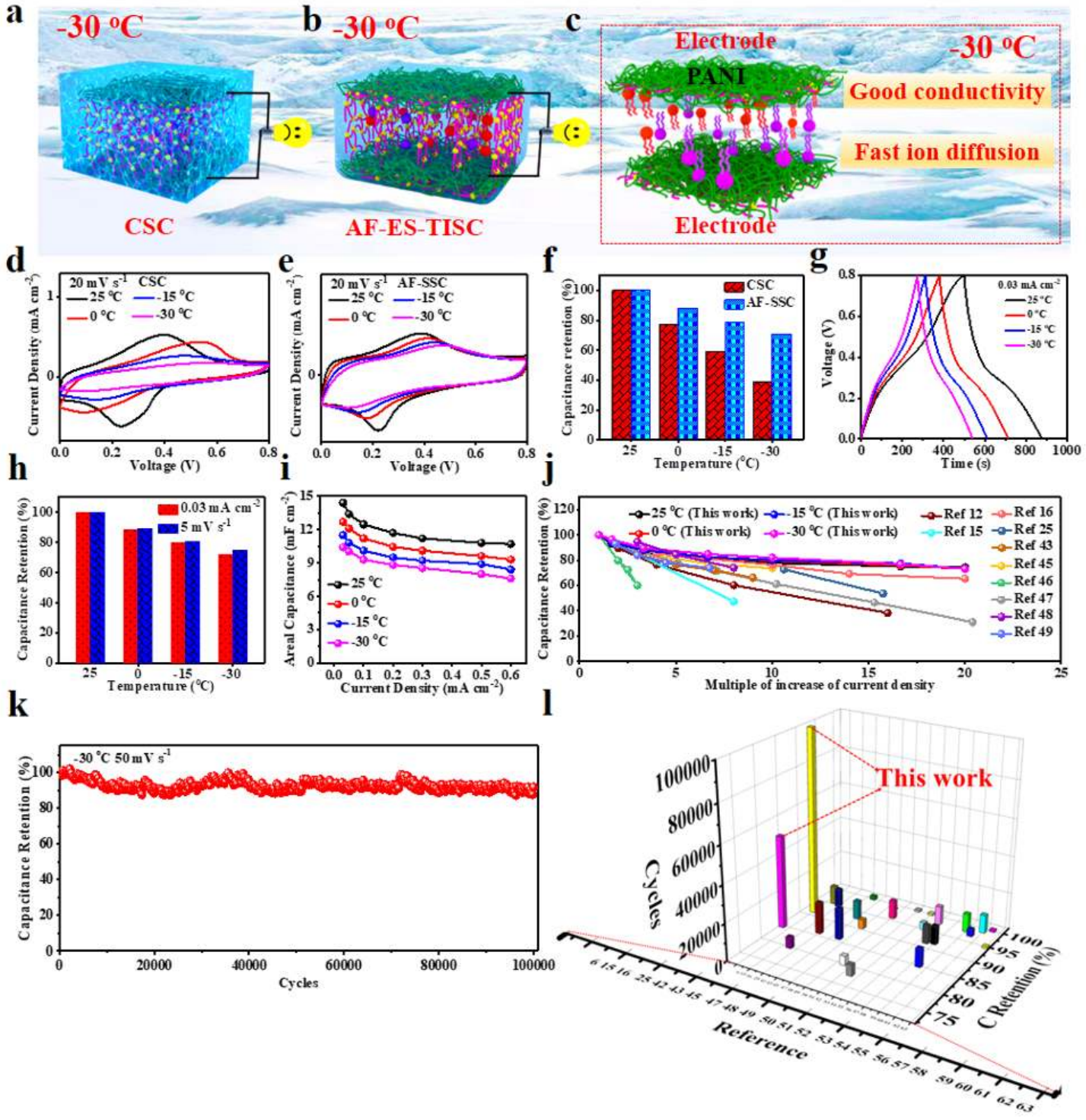

Figure 5

The anti-freezing property of the AF-SSC. a) Schematic illustration of the frozen CSC at -30 oC. b) Schematic diagram of normal operation of AF-SSC at -30 oC. c) Schematic diagram of mechanism of AF-SSC at the low temperature. d) The capacitance retention under different temperature of the integrated CSC, CSC-1/3, AF-SSC, CSC-3/1 when the volume ratios of EG/W are 0, 1/3, 1/1, 3/1, respectively. e) CV curves, f) GCD profiles and g) The capacitance retention under different temperature of AF-SSC. h) GCD

profiles at -30 oC and i) Rate performance under different temperature of AF-SSC. j) The high capacitance retention of AF-SSC as the multiple increase of current density from -30 oC to 25 oC, superior to those of the previously reported SSCs based on pseudocapacitive materials at room temperature12,15,16,43, 25,43-48. k) Cycle performance at 50 mV s-1 of AF-SSC under -30 oC. l) Contrast of cycling stability between AF-SSC at -30 oC and 25 oC in this work and all the previously reported SSCs at room temperature 6, 15, 16, 25, 43, 44, 46-63.

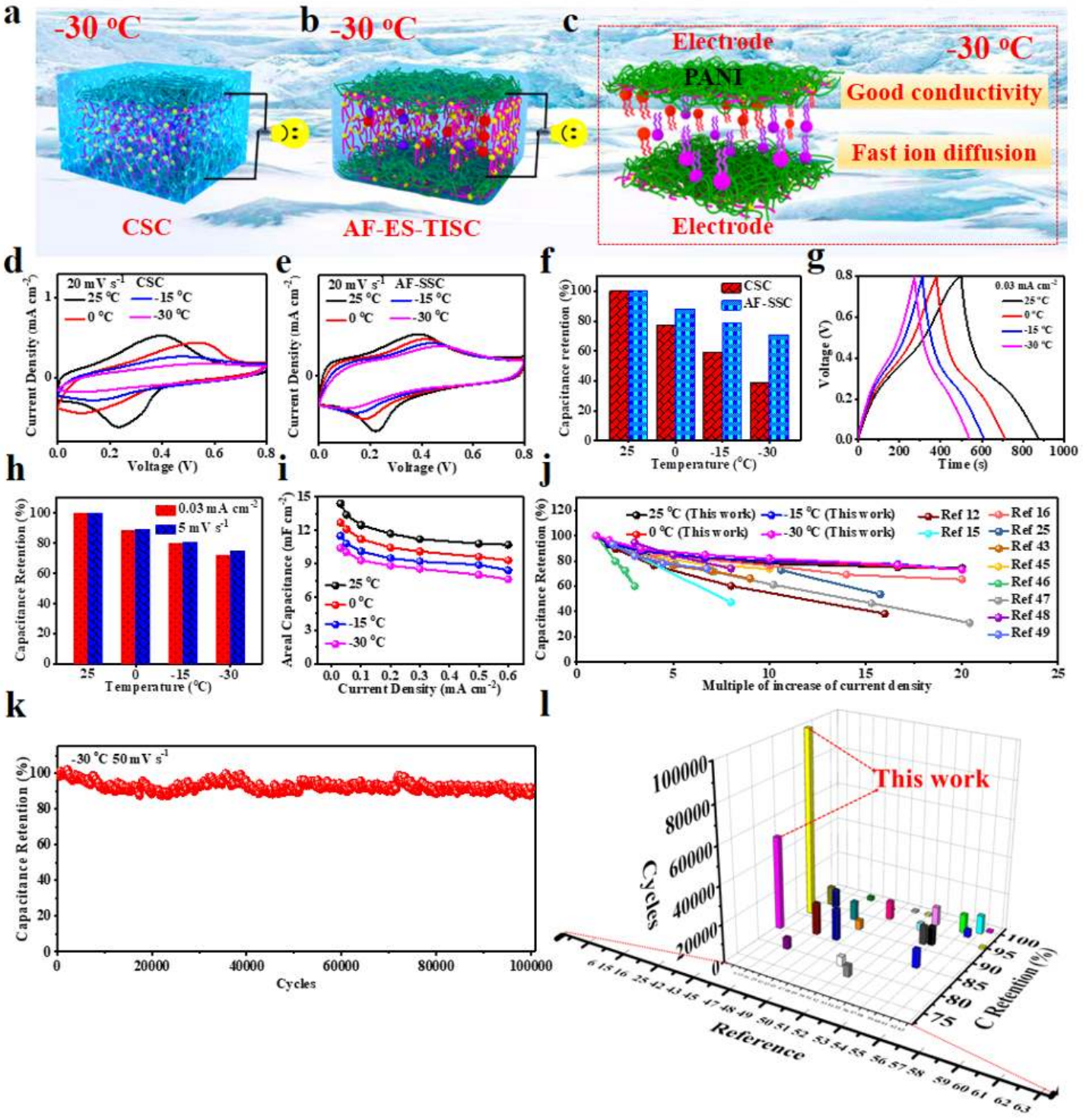

Figure 5

The anti-freezing property of the AF-SSC. a) Schematic illustration of the frozen CSC at -30 oC. b) Schematic diagram of normal operation of AF-SSC at -30 oC. c) Schematic diagram of mechanism of AF-SSC at the low temperature. d) The capacitance retention under different temperature of the integrated CSC, CSC-1/3, AF-SSC, CSC-3/1 when the volume ratios of EG/W are 0, 1/3, 1/1, 3/1, respectively. e) CV curves, f) GCD profiles and g) The capacitance retention under different temperature of AF-SSC. h) GCD profiles at -30 oC and i) Rate performance under different temperature of AF-SSC. j) The high capacitance retention of AF-SSC as the multiple increase of current density from -30 oC to 25 oC, superior to those of the previously reported SSCs based on pseudocapacitive materials at room temperature12,15,16,43, 25,43-48. k) Cycle performance at 50 mV s-1 of AF-SSC under -30 oC. l) Contrast of cycling stability between AF-SSC at -30 oC and 25 oC in this work and all the previously reported SSCs at room temperature 6, 15, 16, 25, 43, 44, 46-63.

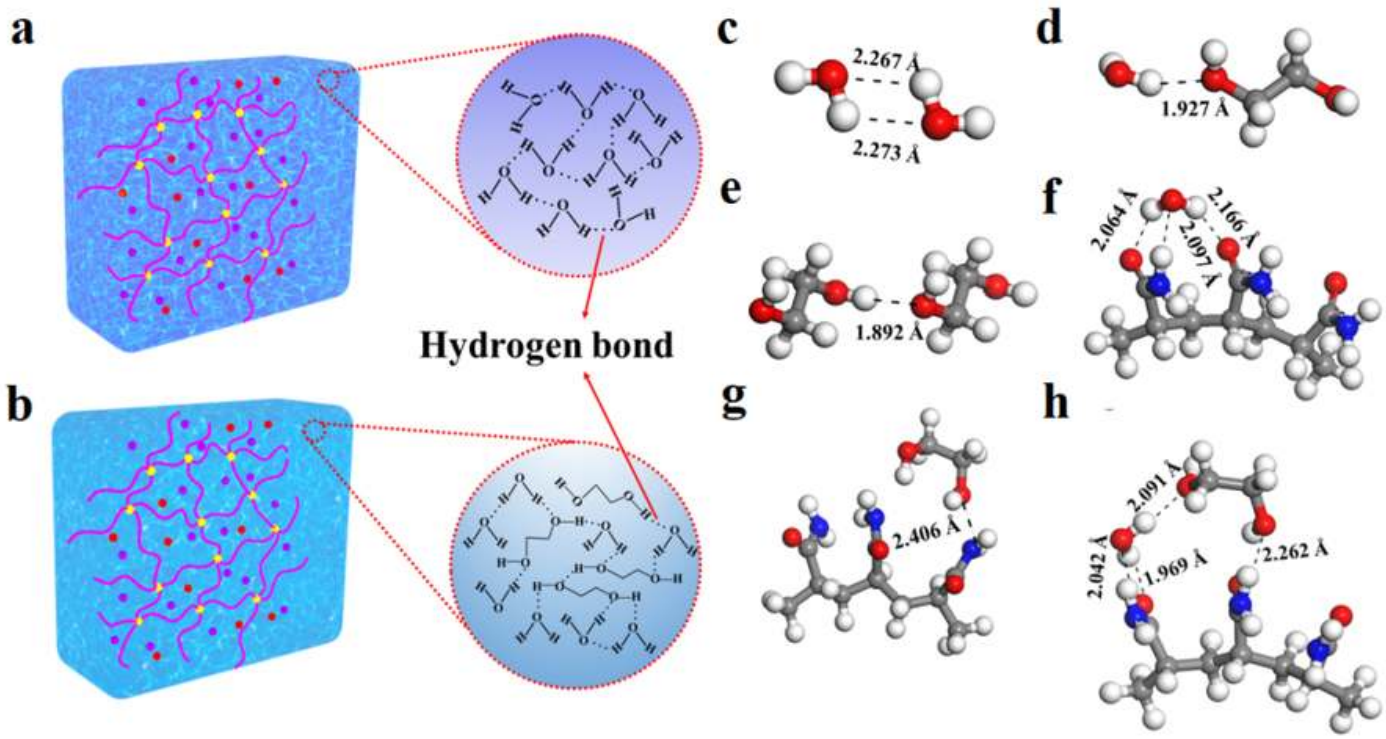

Figure 6

Density functional theory (DFT) analysis. The hydrogen bonding a) between W and W and b) EG and W. The hydrogen-bonding interactions of c) W/W, d) W/EG, e) EG/EG, f) W/PAM, g) EG/PAM and h) W/EG/PAM.

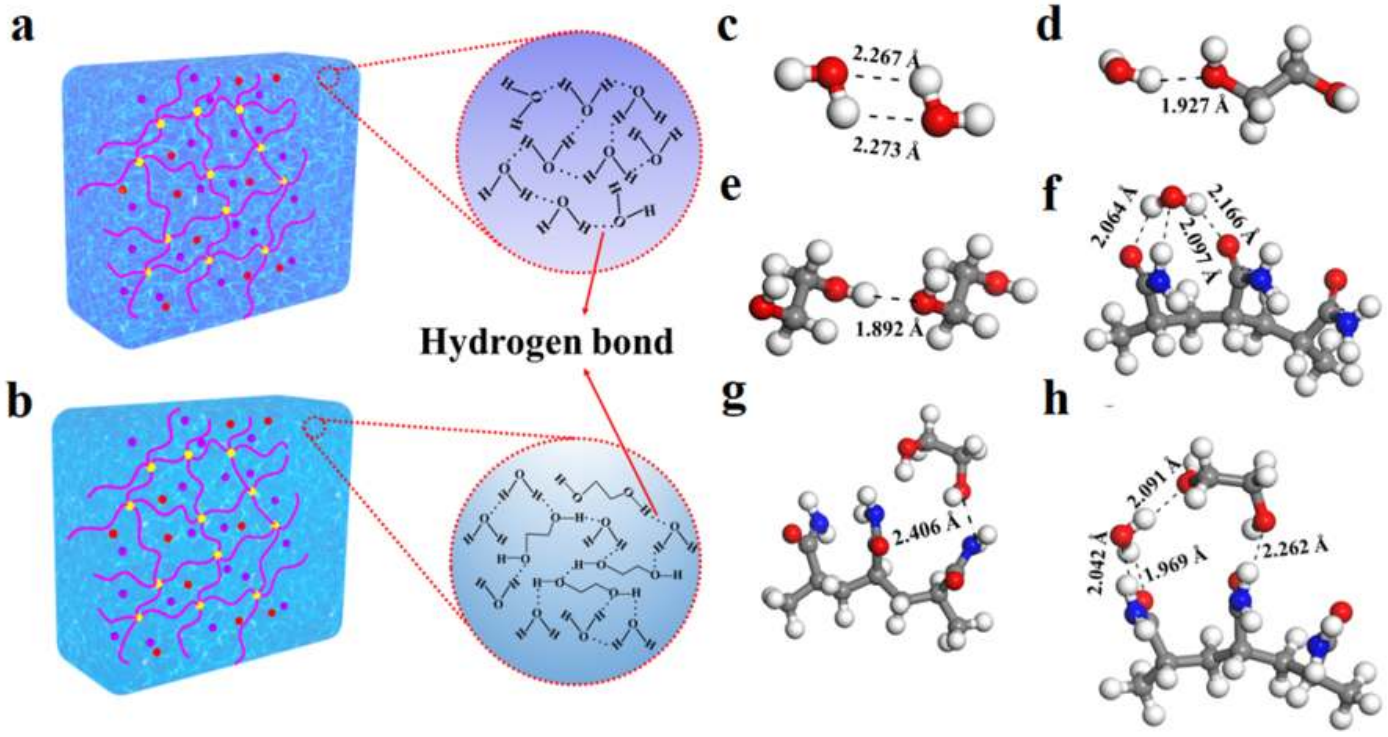

Figure 6

Density functional theory (DFT) analysis. The hydrogen bonding a) between W and W and b) EG and W. The hydrogen-bonding interactions of c) W/W, d) W/EG, e) EG/EG, f) W/PAM, g) EG/PAM and h) W/EG/PAM.

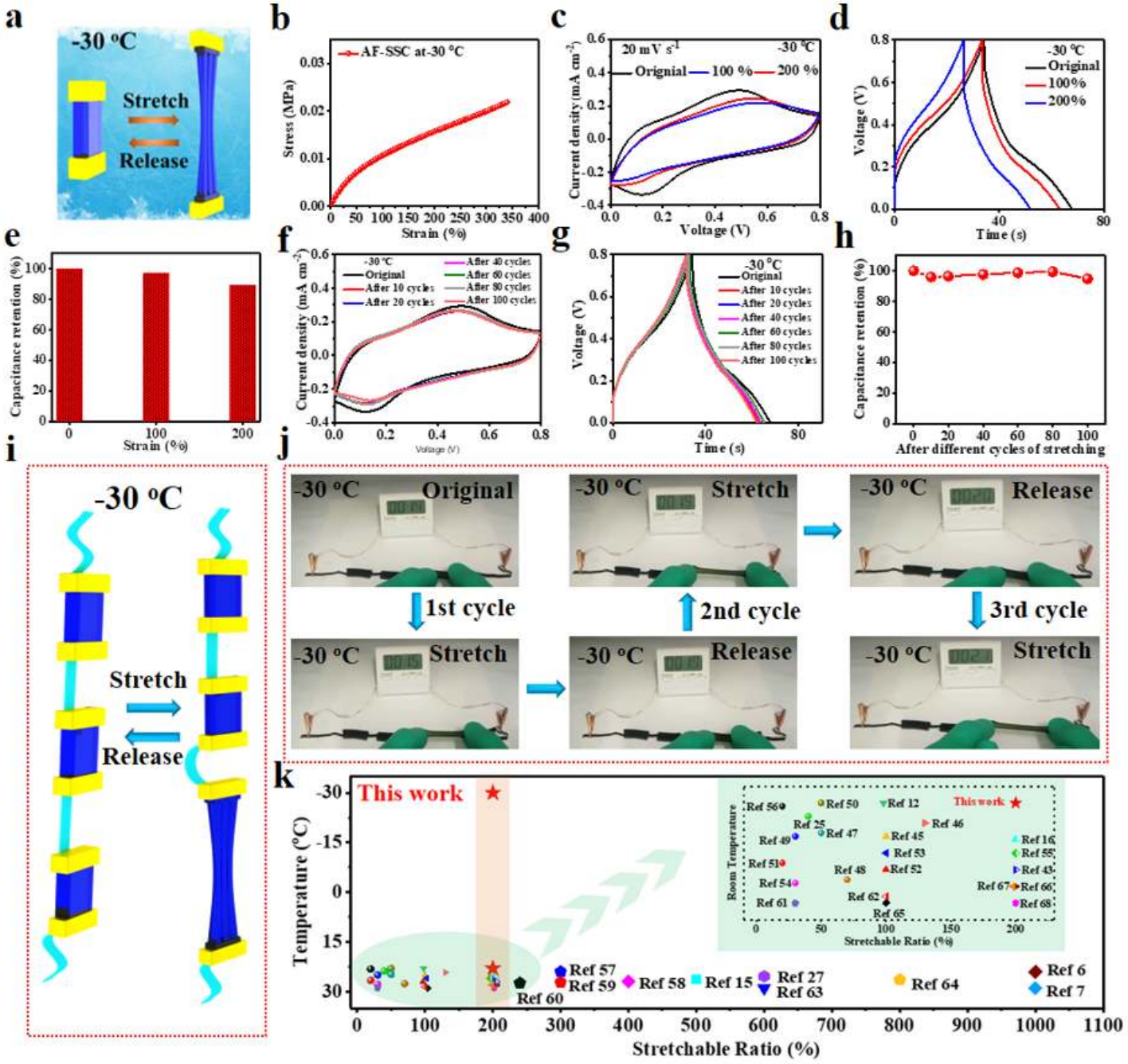

Figure 7

The intrinsic stretchability of AF-SSC under -30 oC. a) Schematic illustration of AF-SSC under stretching at -30 oC. b) Stress-strain curve of AF-SSC at -30 oC. c) CV curves at 20 mV s-1, d) GCD profiles at the current density of 0.2 mA cm-2 and e) Capacitance retention of AF-SSCs under different stretch ratio at -30 oC. f) CV curves at 20 mV s-1, g) GCD profiles at the current density of 0.2 mA cm-2 and h) Capacitance retention of AF-SSC after different stretch/release cycles from the initial to 100% under -30 oC. i) Schematic illustration of three AF-SSCs connected in series under stretching at -30 oC. j) A commercialized timer powered by in-series AF-SSCs under repeatedly stretching at -30 oC. k) The stretch

ratio comparison of AF-SSC and all previously reported SSCs6, 7, 12, 15, 16, 25, 27, 43-63, 65-68 at different temperature range.

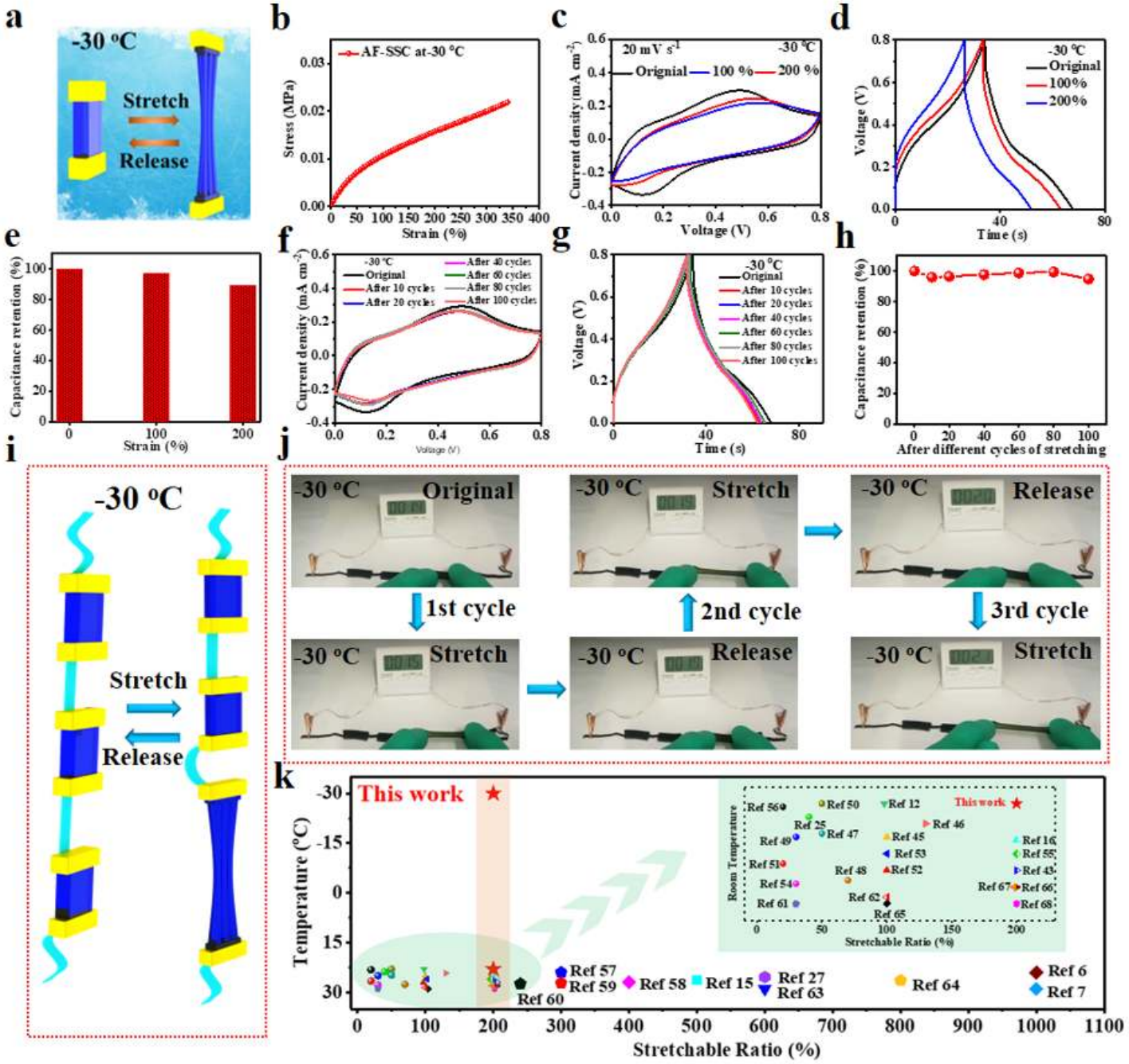

Figure 7

The intrinsic stretchability of AF-SSC under -30 oC. a) Schematic illustration of AF-SSC under stretching at -30 oC. b) Stress-strain curve of AF-SSC at -30 oC. c) CV curves at 20 mV s-1, d) GCD profiles at the current density of 0.2 mA cm-2 and e) Capacitance retention of AF-SSCs under different stretch ratio at -30 oC. f) CV curves at 20 mV s-1, g) GCD profiles at the current density of 0.2 mA cm-2 and h) Capacitance retention of AF-SSC after different stretch/release cycles from the initial to 100% under -30 oC. i) Schematic illustration of three AF-SSCs connected in series under stretching at -30 oC. j) A

commercialized timer powered by in-series AF-SSCs under repeatedly stretching at -30 oC. k) The stretch ratio comparison of AF-SSC and all previously reported SSCs6, 7, 12, 15, 16, 25, 27, 43-63, 65-68 at different temperature range.

Supplementary Files

This is a list of supplementary files associated with this preprint. Click to download.

- SupplementaryMovie1.avi
- SupplementaryMovie1.avi
- SupplementaryMovie2.avi
- SupplementaryMovie2.avi
- SupplementaryMovie3.avi
- SupplementaryMovie3.avi
- SupplementaryMovie4.avi
- SupplementaryMovie4.avi
- SupportingInformation.docx
- SupportingInformation.docx